2015 IEEE International Conference on Robotics and Automation (ICRA)
Washington State Convention Center
Seattle, Washington, May 26-30, 2015

Adaptive Robust Wing Trajectory Control and Force Generation of Flapping Wing MAV

Jian Zhang, Bo Cheng, Bin Yao and Xinyan Deng

Abstract— **The prominent maneuverability of flapping flight is enabled by rapid and significant changes in aerodynamic forces, which is a result of surprisingly subtle and precise changes of wing kinematics. The high sensitivity of aerodynamic forces to wing kinematic changes demands precise and instantaneous control of the flapping wing trajectories, especially in the presence of various types of uncertainties. In this work, we first present a dynamic model of a pair of direct-motor-driven flapping wings while taking into consideration the parameter uncertainties and external disturbances. We then present an Adaptive Robust Controller (ARC) to achieve robust performance of high-frequency (over 30Hz) instantaneous wing trajectory tracking with onboard feedback. The proposed control algorithm was experimentally validated on a 7.5 gram flapping-wing MAV which showed excellent tracking of various wing trajectories with different amplitude, bias, frequency, and split-cycles. Experimental results on various model wings demonstrated that the ARC can adapt to unknown parameters and show no performance degradation across wings of different geometries. The results of ARC were also compared with those of open-loop and classical PID controllers.**

I. INTRODUCTION

The design of Flapping Wing Micro Aerial Vehicles (FWMAVs) was inspired by the prominent maneuverability and stability of insects and hummingbirds [1], [2], due to their abilities to make precise and subtle changes of wing kinematics that result in rapid and significant changes of aerodynamic forces [2]. However, the high sensitivity of aerodynamic forces to wing kinematic changes demands precise and instantaneous control of the flapping wing kinematic trajectories. Nevertheless natural flyers master wing kinematics control in spite of varying parameters [3] and unexpected disturbances [4]. Parameters of flapping wing can be altered by changes of wing size, weight, wear and tear, wind conditions, and variations of air density. External disturbances can be of various forms, such as wind gusts, rain drops, obstacles, etc. Insects and hummingbirds are able to cope with these disturbances and recover their flight stability with ease [4]. It has been shown that the basic wing trajectory of some species of insects is driven by Central Pattern Generator (CPG) in an adaptive feedforward manner [3] and then modified by sensory feedback control.

The impact of uncertainties on the small-scale FWMAVs is substantially larger compared to that on the traditional larger-scale aerial vehicles. In addition, manufacturing imperfections and wear and tear induced by high frequency oscillation call for advanced control algorithms to deal with model uncertainty and varying parameters, which is of critical importance in achieving high stability and maneuverability of a FWMAV.

Based on wing actuation and transmission mechanisms, FWMAV platforms to date can be divided into two main categories: direct-drive type [5]–[7], etc. and linkage type [8]–[10], etc. Compared to the direct-drive systems, the linkage transmission systems are often subjected to kinematics control limitations such as fixed wing trajectories when operating without additional control mechanisms and asymmetry in the kinematics when operating without additional variable speed control [11]. Therefore, force control is limited to varying wing speed profile (e.g., split-cycle) and additional mechanisms are required to further modulate the wing trajectory and angle of attack [8], which could drastically increase the design complexity and becomes infeasible at high frequency. As for the direct drive type, the limitations on fixed and asymmetric wing trajectories are alleviated, and more flexible kinematic control approaches are at our disposal. For example, prior works such as [6], [12] presented modeling and control of wing kinematics of direct drive type FWMAV using open-loop or closed-loop approaches. Due to the size limitation of a feedback sensor at sub-gram scale, Perez-Arancibia and his coworkers [12] used the open-loop feedforward method which achieved excellent control of aerodynamic forces and torques. Also in [13], a combined repetitive and minimum-variance adaptive control strategy was used to generate desired flapping trajectories. In a recent study [6], Zhang et al. demonstrated onborad feedback control using a small magnetic encoder ($1mm \times 1mm$) for wing trajectory feedback. A linear controller was designed and the inherent nonlinearity of the system was treated as disturbance, which limited the achievable control performance.

Inspired by insect wing trajectory control strategy of adaptive feedforward and robust feedback, we proposed a nonlinear Adaptive Robust controller (ARC) [14] and implemented the algorithm on a 7.5 gram FWMAV. The experiments showed that ARC was able to achieve excellent tracking of various wing trajectories (with varying amplitude, bias, frequency and split-cycles) and excellent uncertainties rejection performance. When the system parameters were modified by swapping the original identified wing to a wing with different parameters that are unknown to the controller, the ARC showed no performance degradations, compared to

Research supported by Air Force Research Lab (AFRL). J. Zhang, B. Yao and X. Deng are with the School of Mechanical Engineering, Purdue University.(contact email: xdeng@purdue.edu). Bin Yao is also a Chang Jiang Chair Professor at the State Key Laboratory of Fluid Power Transmission and Control of Zhejiang University in China.

B. Cheng is now with the Department of Mechanical and Nuclear Engineering, Pennsylvania State University.

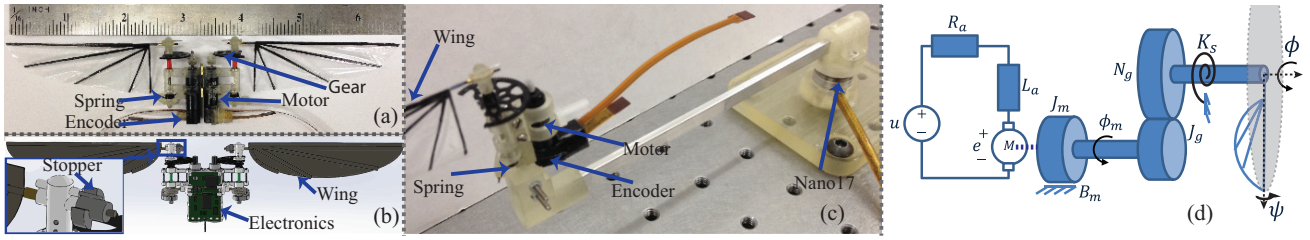

Fig. 1. (a) Assembled FWMAV. (b) Solidworks model of the FWMAV and the wing stopper. (c) Single wing test setup. (d) The diagram of flapping wing actuation system consists of motor with voltage input u, resistance R_a, inductance L_a, back EMF e, motor moment of inertia J_m, damping B_m, and angle ϕ_m, gear with gear ratio N_g, gear moment of inertia J_g, torsion spring with spring constant K_s, and wing with stroke angle ϕ, and rotation angle ψ.

a benchmarking PID controller. Compared with the open-loop method, ARC showed improved force generation results.

II. PROBLEM FORMULATION

A. Flapping Wing System

The experimental setup for single wing testing platform and the assembled FWMAV is shown in Fig. 1(a)(b). The flapping wings are directly driven by two 2.5 gram, 6mm brushless DC motors (FAULHABER, Clearwater, Florida USA) coupled with torsional springs for kinetic energy restoring. Using a gear transmission, the motor was designed to generate an overall reciprocal motion of the wing. The frame structure, wing stopper, wing, and spring holders were prototyped by 3D printing using a multipurpose transparent resin. A portion of the gear on the load shaft was removed to reduce the weight and moment of inertia. Two miniature ball bearings were used to support the load shaft. A pair of torsion springs was mounted on the bottom of the shaft and oriented in such a way that rotation to one direction compresses one spring and extends the other. The wing was allowed to passively rotate, up to a 45 degrees angle limited by a stopper fixed at the proximal end of the wing leading-edge spar. The assembled FWMAV with weight of 7.5 grams and wing span of 15cm is capable of taking off, therefore the current results can be directly implemented on this FWMAV for its flight control.

B. Flapping Wing Dynamic Model

Assuming the inductance of the motor is negligible, the equation of motion for the system (including motor, transmission and wing) is given by [6]

$$J_s\ddot{\phi}+B_{s1}\dot{\phi}+B_{s2}|\dot{\phi}|\dot{\phi}+K_s\phi+T_f sign(\dot{\phi})+\Delta = K_u u \quad (1)$$

where ϕ is the flapping/stroke angle in rad, J_s is the total moment of inertia, B_{s1} and B_{s2} represent the lumped linear and aerodynamic damping coefficients respectively, K_s is the torsional spring coefficient, $T_f sign(\dot{y})$ is the nonlinear friction, K_u is the lumped control input gain, and Δ is a lumped uncertain nonlinearities presenting unstructured nature of disturbances and modeling errors. The modeling of aerodynamics, especially due to the unsteady nature of the flapping wings, is subject to relatively large modeling errors [1] when quasi-steady model is used.

In equation (1), $J_s = N_g^2 J_m + J_w + J_g$, in which N_g is the gear ratio and J_m, J_w and J_g are the moments of inertia of the motor's rotational components, the wing, and the gears respectively. $J_w = \rho_w R_w^3 \bar{c} \hat{r}_2^2(S)$ with ρ_w, R_w, $\bar{c}$ and $\hat{r}_2^2(S)$ being the wing density, the wing length, the wing mean chord length and the 2^{nd} dimensionless moments of wing area [15] respectively. $B_{s1} = N_g^2(B_{m1} + \frac{K_a^2}{R_a})$, in which B_{m1} is the linear damping of the motor's rotational components, K_a is the torque constant, and R_a is the winding resistance. $B_{s2} = 0.5\rho_{air}\overline{C_D}R_w^4\bar{c}\hat{r}_3^3(S)$, where ρ_{air} is air density, $\overline{C_D}$ is the mean drag coefficient and $\hat{r}_3^3(S)$ is the 3rd dimensionless moments of wing area [15]. The aerodynamic drag $B_{s2}|\dot{\phi}|\dot{\phi}$ is estimated based on a quasi-steady aerodynamic model using blade element theory (BET) [1], and $\overline{C_D}$ is the mean drag coefficient averaged over one wing stroke estimated by [1] $\overline{C_D} = \overline{1.92 - 1.55cos(2.04\alpha - 9.82)}$, where the angle of attack α is assumed to be fixed at 45 degrees. The input gain is $K_u = N_g \frac{K_a}{R_a}$. Note that the quasi-steady model is used here due to the lack of simple closed form for unsteady aerodynamic models [1]. The actuation system diagram for one wing is shown in Fig. 1(d).

C. Sensitivity of Force and Torque Generation to Wing Kinematics

For controller design and control performance evaluation, it is necessary to precisely quantify the high sensitivity of the force and torque generation to wing kinematics. The stroke-averaged forces and torques under consideration are F_z, F_x, roll torque T_x, pitch torque T_y and yaw torque T_z defined similar to [16] as shown in Fig. 2. With a fixed angle of attack α, the flapping kinematics of each wing are uniquely defined through its stroke angle, which is assumed to be generated by

$$\phi_i = \begin{cases} A_i cos\left(\frac{2\pi f t}{2\sigma_i} + \psi_i\right) + \phi_{0i}, & if\ 0 \le t < \frac{\sigma_i}{f} \\ A_i cos\left(\frac{2\pi f t - 2\pi}{2(1-\sigma_i)} + \psi_i\right) + \phi_{0i}, & if\ \frac{\sigma_i}{f} \le t < \frac{1}{f} \end{cases} \quad (2)$$

where i represents the right ($i = r$) and left wing ($i = l$), A_i is the flapping amplitude, ψ_i is the phase angle, ϕ_{0i} is the bias angle, and σ_i is the split cycle parameter.

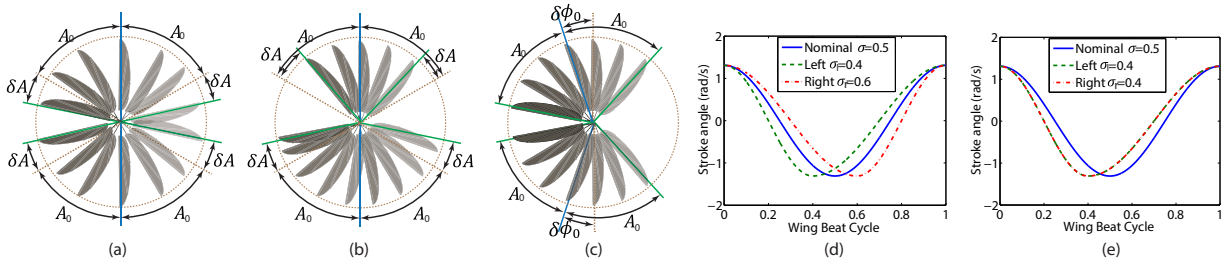

Fig. 3. (a) Symmetric amplitude changes (δA) of left and right wing for lift F_z. (b) Asymmetric amplitude changes (δA) of left and right wing for roll torque T_x. (c) Bias changes ($\delta\phi_0$) of left and right wing for pitch torque T_y. (d) Anti-symmetric split cycle changes ($\delta\sigma$) of left and right wing for F_x. (e) Symmetric split cycle changes ($\delta\sigma$) of left and right wing for yaw torque T_z.

The stable hovering condition of $A_i = A_0$, $\psi_i = 0$, $\phi_{0i} = 0$ and $\sigma_i = 0.5$ is assumed as the nominal kinematics. Under this condition, $F_x = F_y = 0$, $T_x = T_y = T_z = 0$, and the lift generated by the wing pair is balanced by the body weight mg of the MAV/insect, i.e., $mg = \frac{1}{2}\rho_{air}\overline{C_L}R_w^3\bar{c}\hat{r}_2^2(S)\omega_w^2 A_0^2$, where $\overline{C_L}$ is the mean lift coefficient averaged over one wing stroke [1], and $\omega_w = 2\pi f$ is the wing angular velocity.

Sensitivities are defined when kinematic parameters are deviated from their nominal values. Based on the assumption of near-hovering condition and the method in [11] [16], for small deviations from the nominal kinematics parameters in amplitude δA, bias $\delta\phi_0$, and split cycle $\delta\sigma$, it can be shown that

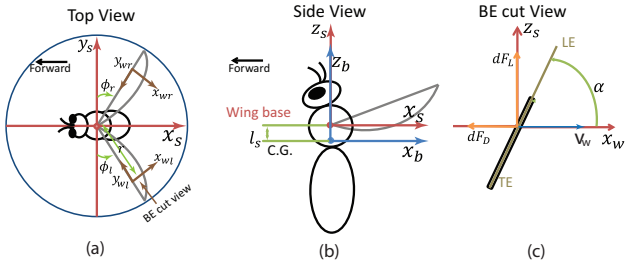

Fig. 2. Schematic view of coordinate systems and kinematics. (a) Top View shows the stroke plane coordinate frame (red) (x_s, y_x, z_s) that originated from wing base. Wing kinematics are specified by the stroke angle ϕ. The positive direction of ϕ is defined to be upstroke direction for both left and right wing. Wing coordinate frames (brown) (x_{wl}, y_{wl}, z_s) and (x_{wr}, y_{wr}, z_s) share the same z direction with stroke plane frame and are attached to the blade element (BE) on the wing at distant r from the wing base. (b) Body coordinate frame (blue) (x_b, y_b, z_b) has the same orientation as the stroke plane frame but with the origin that is located at the center of mass. The offset between wing base and center of mass is l_s. The forces (F_x, F_y, F_z) and torques (T_x, T_y, T_z) that are produced by the wing pair are defined with respect to the stroke frame. (c) Blade element (BE) cut view shows the (geometric) angle of attack α, which is defined as the angle between the wing chord and the tangential of the wings trajectory (relative to the stroke plane), and instantaneous lift dF_L and drag forces dF_D on the BE.

1) The lift force F_z is due to symmetric amplitude changes of the left and right wing, i.e., $A_l = A_0 + \delta A$ and $A_r = A_0 + \delta A$, as shown in Fig. 3(a), is $\delta F_z = \frac{1}{2}\rho_{air}\overline{C_L}R_w^3\bar{c}\hat{r}_2^2(S)\omega_w^2 A_0^2\left(\frac{2\delta A}{A_0}\right)$.

2) The roll torque T_x due to asymmetric amplitude changes of the left and right wing, i.e., $A_l = A_0 + \delta A$ and $A_r = A_0 - \delta A$, as shown in Fig. 3(b), is $\delta T_x = \frac{1}{2}\rho_{air}\overline{C_L}R_w^3\bar{c}\hat{r}_2^2(S)\omega_w^2 A_0^2 r_{cp}\left(\frac{2\delta A}{A_0}\right)$, where $r_{cp} = \frac{\hat{r}_3^3(S)}{\hat{r}_2^2(S)}R_w$ is the center of pressure on the wing.

3) The pitch torque T_y due to symmetric bias changes of the left and right wing, i.e., $\phi_{0l} = \delta\phi_0$ and $\phi_{0r} = \delta\phi_0$, as shown in Fig. 3(c), is $\delta T_y = -r_{cp}F_z sin(\delta\phi_0)$.

4) The yaw torque T_z cannot be realized by the amplitude and bias change, so the split cycle method introduced in [11] is adopted here to generate yaw torque and longitudinal horizontal force F_x. Specifically, when the left and right wing are anti-symmetric for split cycle, i.e., $\sigma_l = \sigma$ and $\sigma_r = 1 - \sigma$, as shown in Fig. 3(d), it can be shown that $\delta T_z = \frac{1}{8}\rho_{air}\overline{C_D}R_w^4\bar{c}\hat{r}_3^3(S)\omega_w^2 A_0^2\left(\frac{1-2\sigma}{\sigma(1-\sigma)}\right)$, where $\sigma = 0.5 - \delta\sigma$, for small $\delta\sigma$, $\left(\frac{1-2\sigma}{\sigma(1-\sigma)}\right) \approx \frac{2\delta\sigma}{0.25} = 8\delta\sigma$.

5) Similarly, longitudinal horizontal force F_x can be generated with symmetric split cycle on the left and right wings, i.e., $\sigma_l = \sigma_r = \sigma$ and $\sigma = 0.5 - \delta\sigma$, as shown in Fig. 3(e): $\delta F_x = \frac{1}{4}\rho_{air}\overline{C_D}R_w^3\bar{c}\hat{r}_2^2(S)\omega_w^2 A_0^2 C_{scx}\left(\frac{1-2\sigma}{\sigma(1-\sigma)}\right)$, where $4C_{scx}\frac{\overline{C_D}}{\overline{C_L}} \approx 1.5$ and $\frac{\overline{C_D}}{\overline{C_L}} \approx 1$.

TABLE I
WING KINEMATIC SENSITIVITY FUNCTIONS

Forces	Kinematics	Sensitivity
F_z	Amplitude	$S_{Fz\|A} = \delta F_z/(\delta A/A_0) = 2mg$
F_x	Split Cycle	$S_{Fx\|\delta\sigma} = \delta F_x/\delta\sigma = 1.5mg$
T_x	Amplitude	$S_{Tx\|A} = \delta T_x/(\delta A/A_0) = 2r_{cp}mg$
T_y	Bias	$S_{Ty\|\delta\phi_0} = \delta T_y/\delta\phi_0 = -r_{cp}mg$
T_z	Split Cycle	$S_{Tz\|\delta\sigma} = \delta T_y/\delta\sigma = 2r_{cp}mg$

From 1)-5) and $mg = \frac{1}{2}\rho_{air}\overline{C_L}R_w^3\bar{c}\hat{r}_2^2(S)\omega_w^2 A_0^2$, we can derive all the sensitivity functions summarized in the Table I. To illustrate the large value of sensitivities, consider small change of kinematics, for example, $\frac{\delta A}{A_0} = 6deg/60deg = 0.1$ and $\delta\phi_0 = 5.7deg \approx 0.1$. With such small change of kinematics, we have $\delta F_z = 0.2mg$, $\delta T_x = 0.2mgr_{cp}$ and $\delta T_x = -0.1mgr_{cp}$, i.e. lift has a 20% of variation relative to the body weight, and roll torque and pitch torque all have very large variations. Similar results can be obtained for other parameters and their sensitivities.

III. ADAPTIVE ROBUST CONTROLLER DESIGN

A. ARC Wing Kinematics and Forces Generation

The high sensitivity of aerodynamic force to kinematic changes imposes a stringent requirement on the wing kinematic control in spite of all the uncertainties (parametric uncertainties and uncertain nonlinearities). Proposed method provide following advantages [14]: 1) Guaranteed transient and steady state performance, thus the transient can be as fast as physically permitted. The bandwidth of the controlled wing dynamics can be greatly increased with high (local) gain feedback. 2) Robust control attenuates the uncertain nonlinearities, including disturbances, modelling errors, wing-body velocity interactions, etc, which is more robust compared to other methods such as L1-adaptive control or an indirect method like model predictive adaptive control, etc. 3) Adaptation for parametric uncertainties.

B. Model and Assumptions

Following the design procedure in [14], one rewrite the model (1) in the state space form,

$$\begin{aligned}\dot{x}_1 =& x_2\\ \theta_1\dot{x}_2 =& K_u u - \theta_2 x_2 - \theta_3 x_2^2 sign(x_2)\\ &- \theta_4 x_1 - \theta_6 sign(x_2) - \theta_5 + \tilde{d}\end{aligned} \tag{3}$$

where $x = [x_1, x_2]^T = [\phi, \dot{\phi}]^T$ represents the state vector of stroke angle and angular velocity, and $\tilde{d} = \Delta - d$ is the uncertain nonlinearities with d as the slow changing components of the uncertainty that can be adapted. To linearly parameterize the state space equation in terms of a set of unknown parameters, define $\theta = [\theta_1, \theta_2, \theta_3, \theta_4, \theta_5, \theta_6]^T$ as $\theta_1 = J_s$,$\theta_2 = B_{s1}$,$\theta_3 = B_{s2}$,$\theta_4 = K_s$, $\theta_5 = d$ and $\theta_6 = T_f$.

Assumption 3.1: Both parametric and nonlinear uncertainties are bounded, i.e.,

$$\theta \in \Omega_\theta \triangleq \{\theta :\ \theta_{\min} \le \theta \le \theta_{\max}\}, \widetilde{d} \in \Omega_d \triangleq \left\{\widetilde{d} :\ ||\widetilde{d}|| \le \delta_d\right\} \tag{4}$$

where $\theta_{\min} = [\theta_{1min}, ..., \theta_{pmin}]^T$, $\theta_{\max} = [\theta_{1max}, ..., \theta_{pmax}]^T$ are known constants, the operation $\le$ for two vectors is performed component-wisely, and δ_d is a known bounding function.

Parametric uncertainties are treated by adaptation and projection. Let $\widehat{\theta}$ denote the estimate of θ and $\widetilde{\theta}$ is the estimation error (i.e., $\widetilde{\theta} = \theta - \widehat{\theta}$). In view of (4), the following adaptation law with discontinuous projection modification in [14] can be used

$$\dot{\widehat{\theta}} = Proj_{\widehat{\theta}}(\Gamma\tau) \tag{5}$$

where $\Gamma > 0$ is a diagonal matrix, $\tau \in \mathbb{R}^p$ is a vector of adaptation functions to be synthesized later. The projection mapping $Proj_{\widehat{\theta}}(\bullet) = [Proj_{\widehat{\theta}_1}(\bullet_1), ..., Proj_{\widehat{\theta}_p}(\bullet_p)]^T$ is taken as follows

$$Proj_{\widehat{\theta}_i}(\bullet_i) = \begin{cases} 0 & if\ \widehat{\theta}_i = \theta_{imax}\ and\ \bullet_i > 0\\ 0 & if\ \widehat{\theta}_i = \theta_{imin}\ and\ \bullet_i < 0\\ \bullet_i & otherwise\end{cases}. \tag{6}$$

It can be shown that for any τ, the adaption law (5)-(6) ensures (4) and

$$\widehat{\theta} \in \Omega_\theta \triangleq \left\{\widehat{\theta} : \theta_{imin} \le \widehat{\theta} \le \theta_{imax}\right\} \tag{7}$$

$$\widetilde{\theta}^T(\Gamma^{-1} Proj_{\widehat{\theta}}(\Gamma\tau) - \tau) \le 0,\ \forall\tau. \tag{8}$$

Define a sliding surface

$$p = \dot{e} + k_1 e = x_2 - \dot{y}_d + k_1 e = x_2 - x_{2eq} \tag{9}$$

where $e = x_1 - y_d(t)$ is the output tracking error, $y_d(t)$ is the desired trajectory and k_1 is any positive feedback gain. The goal of making e as small as possible is equivalent to reducing p, since $G_p(s) = \frac{e(s)}{p(s)} = \frac{1}{s+k_1}$ is a stable transfer function. Then

$$J_s\dot{p} = K_u u + \Phi^T\theta + \tilde{d}, \tag{10}$$

$\Phi = [-(\ddot{y}_d - k_1\dot{e}), -x_2, -x_2^2 S_f(x_2), -x_1, -1, -sign(x_2)]^T$.

The following ARC control is proposed:

$$K_u u = u_a + u_s, u_a = -\Phi^T\hat{\theta}, u_s = u_{s1} + u_{s2}, u_{s1} = -k_2 p \tag{11}$$

where u_a is a feedforward model compensation term, u_s is the robust control term, u_{s1} is used to stabilize the nominal system, and u_{s2} is a robust feedback term used to attenuate the effect of model uncertainties. Substituting (11) into (10),

$$J_s\dot{p} + k_2 p = u_{s2} - \Phi^T\tilde{\theta} + \tilde{d} \tag{12}$$

With the Assumption 3.1 and P1, u_{s2} can be synthesized to dominate the model uncertainties from both parametric uncertainties $\tilde{\theta}$ and uncertain nonlinearities $\tilde{d}$, which satisfies the following two conditions: (I)$p(u_{s2} - \Phi^T\tilde{\theta} + \tilde{d}) \le \epsilon$ and (II)$pu_{s2} \le 0$, where ϵ is a design parameter which should be sufficiently small. One example of u_{s2} that satisfies above conditions can be taken as $u_{s2} = -\frac{1}{4\epsilon}h^2 p$, with $h(x,t) = |\Phi|^T|\theta_{max} - \theta_{min}| + \delta_d$. Other designs of u_{s2} can be found in [14].

Transient and steady state tracking performance are obtained with above ARC design (diagram shown in Fig. 4(f)):

Theorem 3.2: If the adaptation function is chosen as $\tau = \Phi p$, the control law guarantees the following as in [14]: (I) In general, all signals are bounded. Furthermore, the positive definite Lyapunov function V_s defined by $V_s = \frac{1}{2}J_s p^2$ is bounded by $V_s \le \exp(-\lambda t)V_s(0) + \frac{\epsilon}{\lambda}[1 - \exp(-\lambda t)]$, with $\lambda = 2k_2/\theta_{1max}$. (II) If after a finite time, there exist parametric uncertainties only (i.e., $\tilde{d} = 0$), in addition to results in 1), zero final tracking error is also achieved, i.e., $e \to 0$ and $p \to 0$, as $t \to \infty$. Proofs are similar to [14]

IV. CONTROL EXPERIMENT RESULTS

Experiments were conducted on dSPACE DS1103 PPC with sampling rate $f_s = 5kHz$. The motor commutation was implemented on a 72 MHz cortex M3 board (NXP Semiconductors) at rate of 50kHz with custom-made drive electronics. The angle feedback signals are obtained by magnetic encoder (FAULHABER Brushless DC-Servomotors 0620B). Two different wing models were used for control

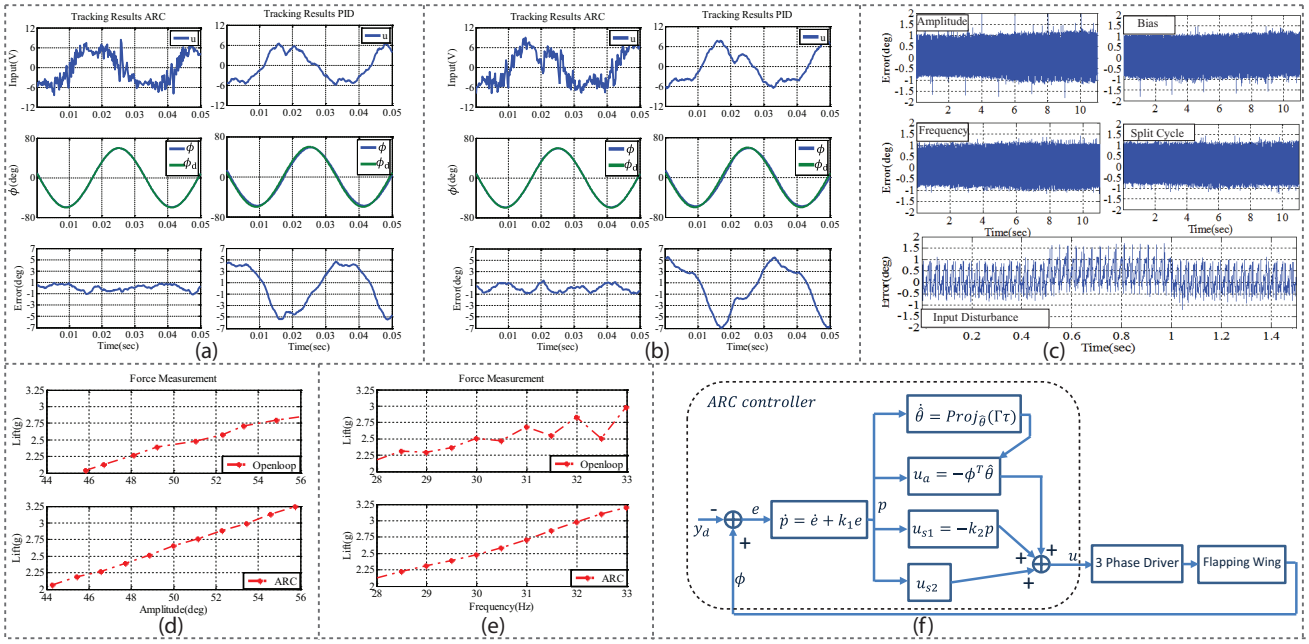

Fig. 4. Tracking performance before (a) and after (b) changes of parameters. (c) ARC tracking errors of different trajectories and with input disturbance. (d) Openloop and ARC lift generation for different amplitudes. (e) Openloop and ARC lift generation for different frequencies. (f) Block diagram of ARC.

experiments with parameters shown in Table II. Least square off-line parameter estimations are performed to obtain the nominal system parameters shown in Table III. Wing #1 was used as the nominal system for controller design, while the parameters of wing #2 are assumed unknown and will be used to demonstrate the controller adaptation. Based on the identified model parameters of the nominal system (wing #1), the ARC control parameters were chosen as $k_1 = 1000$, $k_2 = 200J_s = 3.0920e-5$, and $\epsilon = 0.12$. Specifically, k_1 was chosen to be as large as possible but 5 times smaller than loop sampling frequency f_s to avoid any digital effect. k_2 was chosen according to u_{s1}s contribution to the nominal bandwidth of 200rad/s. ϵ was selected according to the overall desired local bandwidth and the balance between k_2 and ϵ, to avoid control saturation. For parameter adaptation, the initial values were chosen not to be the same as the identified values, but the value shown in Table II as $\hat{\theta}_0$. Adaptation rates $\Gamma = diag(4.5307e-12, 2.9416e{-}08, 6.4701e{-}13, 0.0065, 5e{-}05, 2e{-}07)$ is selected according to general gradient type adaptation method. Bounds for the parameters and the uncertain are chosen to be rather conservative according to the prior knowledge of physical properties. For benchmarking and comparison, a PID controller was also designed based on the identified model parameters of the nominal system (wing #1). Pole placement design techniques were used to obtain PID control parameters K_p, K_i and K_d that achieves closed loop poles at $-250, -250\pm250i$, which is 50rad/s higher than the nominal bandwidth of ARC. Further increasing of bandwidth for PID leads to control saturation and degraded control performance. The PID control with nominal model compensation is used with $u = J_s\ddot{y} + B_{s1}\dot{y} + B_{s2}\dot{y}|\dot{y}| - K_p e - K_i \int e\,dx - K_d\dot{e}$.

TABLE II
WINGS PARAMETERS

Wing	$m(mg)$	$R_w(mm)$	$\bar{c}(mm)$	$\hat{r}_2^2$	$\hat{r}_3^3$	$J_w(mg.mm^2)$
1	62	62.8	11	0.29	0.20	69718
2	66	69.3	16	0.25	0.20	79241

TABLE III
SYSTEM PARAMETERS (SI UNITS)

Wing	J_s	B_{s1}	B_{s2}	K_s	d	T_f
1	1.55e-7	9.60e-6	3.47e-8	6.00e-3	1.22e-4	2.31e-5
2	1.60e-7	9.56e-6	7.48e-8	6.00e-3	1.2e-4	2.30e-5
$\hat{\theta}_0$	1.50e-7	1.00e-5	3.70e-8	5.70e-3	1.00e-4	2.00e-5

A. Kinematics Control Results

The nominal control performance comparison between PID and ARC are shown in Fig. 4(a). The control results show that ARC achieves a tracking error within 1 deg, while the error for PID controller has a peak value of almost 5deg. The presence of the small higher-frequency correction signal is the evidence of ARC's robust control u_{s2} in action, which gives an effective local nonlinear high gain and avoids control saturation associated with linear high gain control. Due to adoption of smoothed version of the robust sliding mode control term u_{s2}, the ARC exhibits little control input chattering.

In order to demonstrate ARC's ability to effectively handle parametric uncertainties through online adaptation, with two controllers remaining unchanged, the nominal wing #1 was swapped with 'unknown' wing #2. The control results after the converged adaptation are shown in Fig. 4(b). Compared with the results of nominal wing (Fig. 4(a)), it is clear that the ARC shows no performance degradation in that there

is no increase of control input level and tracking error. However, the control performance of the non-adapting PID controller deteriorated. With $A/A_0 = 1/60 = 0.017$, The lift generation sensitivity for ARC is $\delta\bar{F}_z = mg(2\delta A/A_0) = 3.3\%mg$, i.e. the maximum lift variation is only 3.3%. For PID, $\delta A/A_0 = 5.5/60 = 0.0917$ and the maximum lift variation is as large as 18.3%. Therefore, the ARC controller is proven to be effective in handling parametric uncertainties and delivering guaranteed robust force generation.

To further prove that the ARC controller is suitable for aerodynamic force generation, the following trajectories are tracked: (T1) amplitude variation, from 54.27deg to 65.73deg; (T2) frequency variation, from 28Hz to 33Hz; (T3) bias, from -0.1rad to 0.1rad; (T4) split-cycle, from 0.45 to 0.55. All trajectory parameters were updated to new values at increments of 1sec. The tracking errors are shown in Fig. 4(c). For all the trajectories, different parameters, and even during the transient portions between parameter updates, the errors are within the consistent range of $\pm 1deg$. Next, the ARCs input disturbance rejection results are shown in Fig. 4(c). A 1V input disturbance was applied at 0.5 sec and removed at 1 sec. The resulting error shows a slight offset from 1deg to 1.5deg, but is still very small. As a comparison, this 1V input results in a larger angle offset around $K_u/K_s \approx 9deg$ in openloop experiments.

B. Lift Force Generation Results

Force measurement was performed using a six component force/torque transducer (Nano17, ATI Ind. Automation). Due to limited resolution of Nano17 (0.3g resolution on the force and 1/64Nmm resolution on the torque measurement), a rigid 150mm beam setup was used to amplify the lift measurement as shown in Fig. 1(c). The improved resolution was about 0.0106g. The force sensor and beam setup was calibrated with precision weights of 0.1g, 0.5g, 5g and 20g and verified the resolution of at least 0.03g. When calculating the time-averaged force, sufficient large number of wing-beat cycles at steady state ware used to guarantee the reliability of the results.

To test the performance of the lift generation from ARC controlled kinematics, lifts at various amplitudes and frequencies were measured and the average lifts obtained are shown in Fig. 4(d) and 4(e). For comparison, the lifts in openloop experiments were also measured and plotted. The amplitude of the open-loop response was matched with the ARC controlled one for fair comparison. The results clearly demonstrate the excellent performance of ARC in aerodynamic force generation with better consistency, accuracy, smoothness and linearity across the tested amplitude and frequency range. In contrast, the open-loop generated force not only varied in an unpredicted way, but also did not generate as much lifts as ARC controlled wing kinematics.

V. Conclusion and Future Work

In this paper, to address the performance robustness issues of flapping wing kinematic trajectory and force generation, we presented an Adaptive Robust Controller (ARC) for instantaneous wing trajectory tracking with onboard feedback of a 7.5 gram direct-drive FWMAV flapping at high-frequency (over 30Hz). The proposed method was experimentally shown to achieve robust tracking of various trajectories with varying amplitude, bias, frequency and split-cycle, with good input disturbance rejection and excellent adaptation capabilities to parameter changes. Experimental results showed improved force control results compared with open-loop method and the PID controller. Future work will focus on the implementation of the ARC wing controller as a subsystem of the vehicle controller to achieve and improve hovering and maneuvering ability.

References

[1] M. H. Dickinson, F.-O. Lehmann, and S. P. Sane, "Wing rotation and the aerodynamic basis of insect flight," *Science*, vol. 284, no. 5422, pp. 1954–1960, 1999.

[2] A. J. Bergou, L. Ristroph, J. Guckenheimer, I. Cohen, and Z. J. Wang, "Fruit flies modulate passive wing pitching to generate in-flight turns," *Physical review letters*, vol. 104, no. 14, p. 148101, 2010.

[3] D. M. Wilson, "The central nervous control of flight in a locust," *The Journal of experimental biology*, vol. 38, no. 47, pp. l–490, 1961.

[4] B. Cheng, X. Deng, and T. L. Hedrick, "The mechanics and control of pitching manoeuvres in a freely flying hawkmoth (manduca sexta)," *The Journal of experimental biology*, vol. 214, no. 24, pp. 4092–4106, 2011.

[5] R. J. Wood, "The first takeoff of a biologically inspired at-scale robotic insect," *Robotics, IEEE Transactions on*, vol. 24, no. 2, pp. 341–347, 2008.

[6] J. Zhang, B. Cheng, J. A. Roll, X. Deng, and B. Yao, "Direct drive of flapping wings under resonance with instantaneous wing trajectory control," in *2013 IEEE International Conference on Robotics and Automation (ICRA)*, May 2013, pp. 4029–4034.

[7] L. Hines, D. Campolo, and M. Sitti, "Liftoff of a motor-driven, flapping-wing microaerial vehicle capable of resonance," *IEEE Transactions on Robotics*, vol. 30, no. 1, pp. 220–232, Feb 2014.

[8] M. Keennon, K. Klingebiel, H. Won, and A. Andriukov, "Development of the nano hummingbird: A tailless flapping wing micro air vehicle," in *AIAA Aerospace Sciences Meeting*, 2012.

[9] G. De Croon, M. Groen, C. De Wagter, B. Remes, R. Ruijsink, and B. Van Oudheusden, "Design, aerodynamics and autonomy of the delfly," *Bioinspiration & biomimetics*, vol. 7, no. 2, p. 025003, 2012.

[10] Z. Khan, K. Steelman, and S. Agrawal, "Development of insect thorax based flapping mechanism," in *Robotics and Automation, 2009. ICRA'09. IEEE International Conference on*. IEEE, 2009, pp. 3651–3656.

[11] D. B. Doman, M. W. Oppenheimer, and D. O. Sigthorsson, "Dynamics and control of a biomimetic vehicle using biased wingbeat forcing functions: Part ii: Controller," *48th AIAA Aerospace Sciences Meeting Including the New Horizons Forum and Aerospace Exposition*, vol. 1024, 2010.

[12] N. O. Pérez-Arancibia, J. P. Whitney, and R. J. Wood, "Lift force control of flapping-wing microrobots using adaptive feedforward schemes," *IEEE/ASME Transactions on Mechatronics*, vol. 18, no. 1, pp. 155–168, 2013.

[13] P. Chirarattananon, N. O. Pérez-Arancibia, and R. J. Wood, "Wing trajectory control for flapping-wing microrobots using combined repetitive and minimum-variance adaptive methods," in *American Control Conference (ACC), 2012*. IEEE, 2012, pp. 3831–3838.

[14] B. Yao, "Advanced motion control: from classical pid to nonlinear adaptive robust control," 2010, pp. 815–829.

[15] C. Ellington, "The aerodynamics of hovering insect flight. ii. morphological parameters," *Philosophical Transactions of the Royal Society of London. B, Biological Sciences*, vol. 305, no. 1122, pp. 1–15, 1984.

[16] B. Cheng and X. Deng, "Translational and rotational damping of flapping flight and its dynamics and stability at hovering," *Robotics, IEEE Transactions on*, vol. 27, no. 5, pp. 849–864, 2011.